

Competing magnetic orders in a bilayer Hubbard model with ultracold atoms

<https://doi.org/10.1038/s41586-020-03058-x>

Received: 25 April 2020

Accepted: 2 October 2020

Published online: 6 January 2021

 Check for updates

Marcell Gall^{1,2}, Nicola Wurz^{1,2}, Jens Samland¹, Chun Fai Chan¹ & Michael Köhl¹✉

Fermionic atoms in optical lattices have served as a useful model system in which to study and emulate the physics of strongly correlated matter. Driven by the advances of high-resolution microscopy, the current research focus is on two-dimensional systems^{1–3}, in which several quantum phases—such as antiferromagnetic Mott insulators for repulsive interactions^{4–7} and charge-density waves for attractive interactions⁸—have been observed. However, the lattice structure of real materials, such as bilayer graphene, is composed of coupled layers and is therefore not strictly two-dimensional, which must be taken into account in simulations. Here we realize a bilayer Fermi–Hubbard model using ultracold atoms in an optical lattice, and demonstrate that the interlayer coupling controls a crossover between a planar antiferromagnetically ordered Mott insulator and a band insulator of spin-singlets along the bonds between the layers. We probe the competition of the magnetic ordering by measuring spin–spin correlations both within and between the two-dimensional layers. Our work will enable the exploration of further properties of coupled-layer Hubbard models, such as theoretically predicted superconducting pairing mechanisms^{9,10}.

The static and dynamical properties of strongly correlated quantum matter are notoriously difficult to understand. Strong quantum correlations often prohibit intuitive models, and the interplay between interactions and kinetic energy gives rise to novel effects, such as quantum magnetism and superconductivity. A particular challenge has been the two-dimensional Hubbard model, which is hard to solve on a computer and bears a number of conceptually open questions. However, the simulation of actual materials is (even) more involved and must go beyond the two-dimensional Hubbard model. Most real materials are not plainly two-dimensional, but possess rather complex lattice structures, which can be approximated as a system of coupled layers.

The simplest realization of a coupled-layer material is the bilayer Hubbard model; see Fig. 1. In addition to the usual elements of the Hubbard model, namely, the tunnel coupling, t , between adjacent lattice sites and the on-site interaction with the energy, U , it contains the tunnel coupling, t_{\perp} , between layers as an independent parameter.

The strength of the tunnel coupling determines the correlations between the two layers. Hence, it has a pivotal role in determining whether antiferromagnetic order in each layer is the dominant configuration or even more exotic phases, not encountered in pure two-dimensional samples, are realized. In the case of strong interlayer tunnel coupling, this includes a band insulator phase of singlet pairs along the bilayer bonds close to half-filling, $n=0.5$ (refs. ^{11–14}). In the $U \rightarrow \infty$ limit, the bilayer Hubbard model maps to the well known Heisenberg model with a critical value of $t_{\perp}/t=1.588$ (ref. ¹⁵), below which the system exhibits antiferromagnetic ordering in the layers and above which the system enters the band insulating phase. For decreasing interaction strength, the critical value of t_{\perp} that marks the crossover from insulator to band insulator is predicted to increase. Numerical simulations

for small systems have revealed that even more exotic phases, such as antiferromagnetic metals, could exist^{11,16}. However, the prime experimental challenge to observe these phases is the difficulty of detection. Whereas two-dimensional Hubbard models are now routinely amenable to high-resolution microscopy^{1–3}, coupled-layer systems face difficulties in read-out because the layers must be microscopically close together to realize a strong and adjustable coupling. Very recently, techniques to overcome this have been presented^{17,18} but the different ground states of the bilayer system have not yet been revealed.

Here, we realize a bilayer Fermi–Hubbard model using ultracold atoms. We employ both fully spin- and density-resolved imaging techniques with high spatial resolution to reveal the density and local magnetic correlations. Using tomographic imaging, we can directly image both layers separately. Moreover, we measure the staggered magnetic correlation function within and between the layers, thereby revealing the antiferromagnetic order. Our results show that the type of magnetic order is highly sensitive to the degree of interlayer coupling and that we can control a crossover between two insulators, a planar antiferromagnetically ordered Mott insulator and a band insulator of spin-singlets, along the bonds between the layers; see Fig. 1a.

Our experimental setup is an extension of our previous work^{3,19}. The starting point for the preparation of the bilayer Hubbard model is a two-species band insulator of atoms in the two lowest hyperfine states of ⁴⁰K, namely, $|\uparrow\rangle = |F=9/2, m_F=-9/2\rangle$ and $|\downarrow\rangle = |F=9/2, m_F=-7/2\rangle$ (where F and m_F are the hyperfine and magnetic quantum numbers, respectively). A 50/50 mixture of these is confined in a two-dimensional optical lattice in the x – y plane with a lattice spacing of $d=532$ nm. Subsequently, we employ a bichromatic optical superlattice in the vertical z direction with wavelengths $\lambda_1=532$ nm and $\lambda_2=1,064$ nm and periods $d_1=1.1$ μ m

¹Physikalisches Institut, University of Bonn, Bonn, Germany. ²These authors contributed equally: Marcell Gall, Nicola Wurz. ✉e-mail: michael.koehl@uni-bonn.de

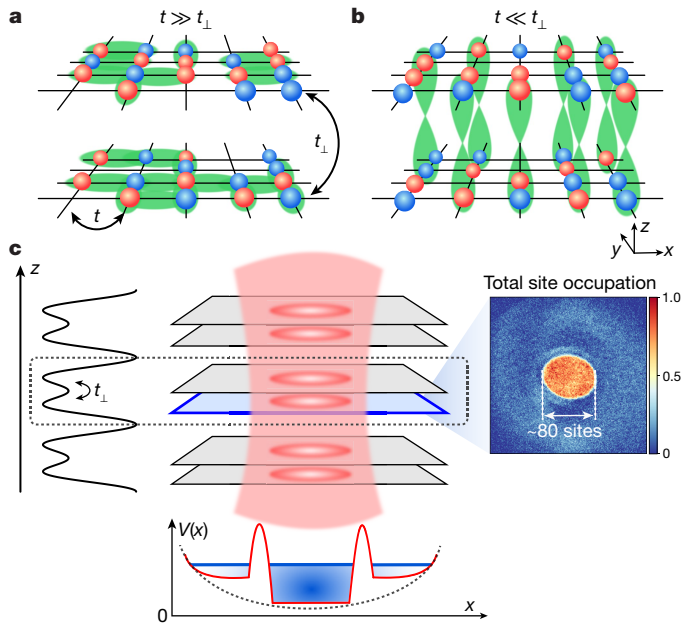


Fig. 1 | Illustration of the bilayer Hubbard model. **a**, For weak interlayer tunnelling ($t_{\perp} \ll t$) the ground state is composed of two weakly coupled two-dimensional antiferromagnetic Mott insulators. The shaded green areas illustrate the spin correlations between spin-up and -down particles, shown as red and blue spheres, respectively. **b**, For strong interlayer coupling ($t_{\perp} \gg t$) the physics is dominated by singlets along the z axis forming an unconventional band insulator; however, antiferromagnetic correlations in the layer disappear. **c**, Experimentally, the bilayer system is realized by a bichromatic superlattice in the z direction trapping atoms in several bilayer sheets. Lateral confinement is provided by optical potentials realizing a flat-bottom trap. Using tomographic imaging, (spin-) densities in a single layer are detected. The inset shows the in situ density of one layer averaged over 12 realizations.

and $d_z = 2.2 \mu\text{m}$, respectively, to split the band insulator into two coupled Mott insulators. During the melting of the band insulator, we allow intralayer tunnelling in the x and y directions by setting the x - y lattice depth to values between $5E_r$ and $7E_r$, leading to tunnelling amplitudes of $t/h = 290$ – 174 Hz. Here, $E_r = \hbar^2/(8md^2)$ denotes the recoil energy for atoms with mass m , and \hbar is Planck's constant. During the splitting procedure, we set the interaction strength to moderately repulsive. Also, we use a spatial light modulator to create a laterally homogeneous trapping potential surrounded by a strong potential barrier that separates regions of low density, which serve as a reservoir for entropy. Our preparation produces a homogeneous bilayer region containing approximately 5,600 sites per layer. For more details, see Methods.

To detect the antiferromagnetic order within one layer, we measure the staggered magnetic structure factor $S(\mathbf{q})$ at wave vector $\mathbf{q} = (\pi/d, \pi/d)$ in a Ramsey-type experiment; see Fig. 2a. To this end, we apply a global $\pi/2$ rotation to all spins, followed by a time evolution in a magnetic field gradient precisely aligned with the diagonal of the x - y lattice. The gradient is applied for a time such that spins separated by a distance of $\sqrt{2}d$ along the diagonal of the lattice rotate their phase by 2π relative to each other. Neighbouring sites along the principal lattice axes therefore experience a differential rotation of π only. A subsequent $\pi/2$ pulse completes the sequence and maps the time-evolved spin state into the measurement basis. The density in both spin states is measured by absorption imaging in the same experimental realization. Subsequently, the spin structure factor is measured by an autocorrelation analysis of the difference of the spin-up and spin-down density¹⁹. We combine the Ramsey spin rotation in each layer of the Hubbard lattice with tomographic resolution in the z direction and thus detect the antiferromagnetic correlations in a single layer of the coupled-bilayer system.

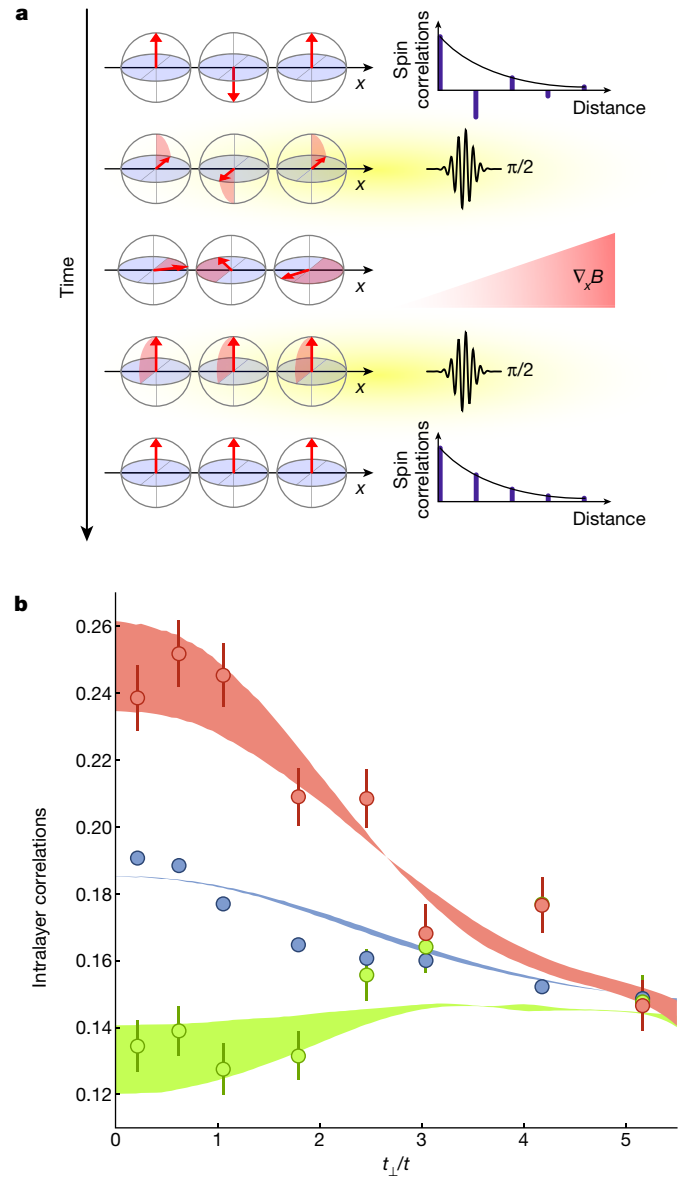


Fig. 2 | Detection of intralayer correlations. **a**, Ramsey sequence in a magnetic field gradient used for the detection of the staggered magnetic structure factor $S(\mathbf{q})$ at wave vector $\mathbf{q} = (\pi/d, \pi/d)$. **b**, Staggered structure factor (red) versus interlayer tunnelling amplitude t_{\perp} . For comparison, we also show the uniform structure factor $S(\mathbf{q} = 0)$ (green) and local magnetic moment (blue). The data were taken with $t = 174$ Hz and $U \approx 8t$. The shaded areas are the results of DQMC calculations corresponding to the experimental parameters covering the temperature range $k_B T = 1.0t$ – $1.4t$ at filling factor $n = 0.4$ (k_B , Boltzmann constant; T , temperature). The error bars denote the standard error of the spin correlation results in the central region of the cloud.

In Fig. 2b, we show the staggered spin structure factor $S[\mathbf{q} = (\pi/d, \pi/d)]$ for various interlayer tunnelling amplitudes t_{\perp} . For reference, we also show the local magnetic moment $C_0 = \langle (\hat{S}_i^z)^2 \rangle - \langle \hat{S}_i^z \rangle^2$, which measures the contribution of purely local magnetic correlations without any long-range contribution. Here, \hat{S}_i^z denotes the spin operator on lattice site i . The local moment is detected by measuring the density of singly occupied lattice sites of the two different spin components separately. Finally, we also show the homogeneous magnetic structure factor $S[\mathbf{q} = (0, 0)]$, which is suppressed because of the antiferromagnetic ordering. The homogeneous magnetic structure factor is measured using the same autocorrelation analysis as for the staggered spin structure factor, but without applying the magnetic field gradient before

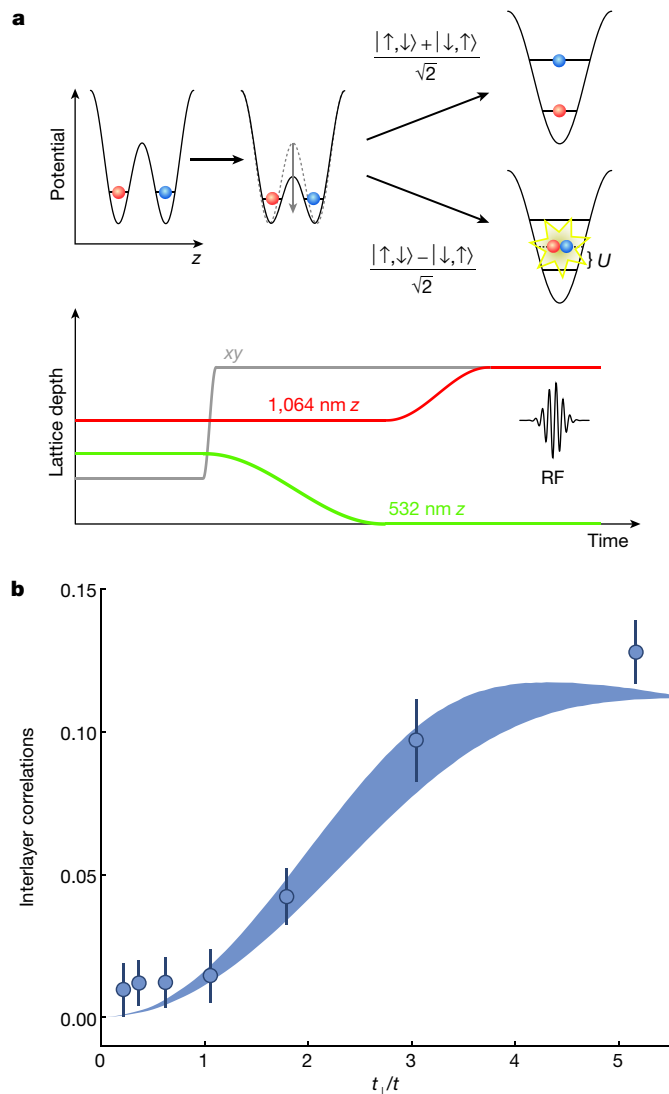


Fig. 3 | Magnetic correlations between the layers. **a**, A double well along the z direction is merged by a suitable ramp of the intensities of the optical superlattice. Only if the double well has been in a spin-singlet configuration do both atoms end up in the vibrational ground state of the merged lattice, which is detected by radiofrequency (RF) spectroscopy. **b**, Staggered spin correlator between the coupled layers of the bilayer system. The data were taken with the same Hubbard parameters as for Fig. 2b. The error bars denote the standard deviation of the interlayer correlations for different realizations. The shaded area shows the DQMC calculations for a temperature range of $k_B T = 1.0t - 1.4t$.

detection; see Methods. For systems without any long-range magnetic correlations, all three correlators should be equal. We compare our experimental results to numerical simulations using the determinant quantum Monte Carlo (DQMC) method (see shaded areas in Fig. 2b). The simulations describe a system with filling factor $n = 0.4$ to account for imperfections—that is, holes—in the initial state and local inhomogeneities of the trap potential. All three magnetic correlators agree very well with the experimental data. At the temperatures reached in our experiment, we do not expect long-range correlations. This is reflected in the fact that the distances of the staggered and uniform structure factors to the local moment are equal, which indicates nearest-neighbour correlations only. In particular, for very large values of t_{\perp} we observe that the homogeneous and staggered structure factors agree within errors, which directly implies that within the layer there are only on-site spin correlations. The intralayer spin correlation data are particularly sensitive to any imperfection in the detection fidelity of the monolayer

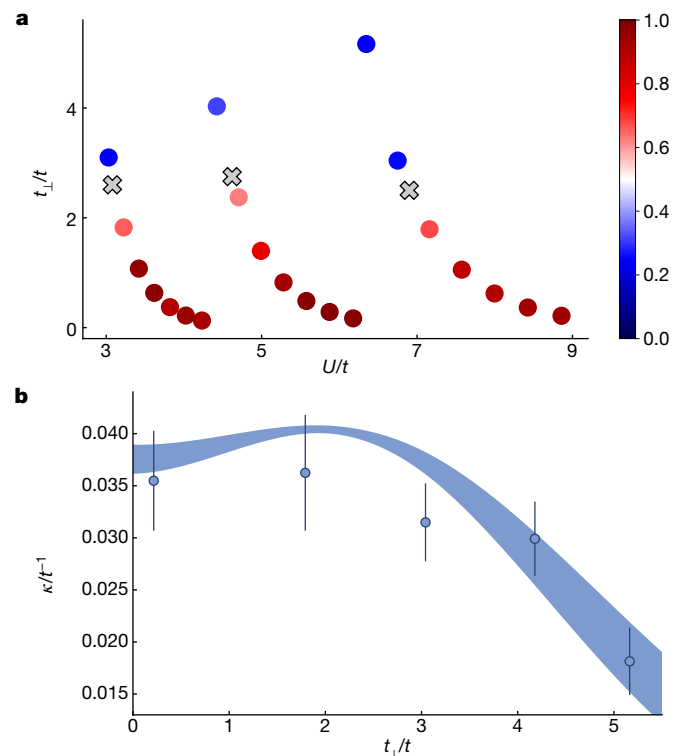


Fig. 4 | Crossover from the antiferromagnetic Mott insulator to a band insulator of singlets. **a**, We plot the ratio R of intralayer to the sum of intra- and interlayer magnetic correlations as a function of both t_{\perp}/t and U/t . The crosses show the interpolated values for $R = 0.5$. The relative standard error on the ratio R is approximately 17%. **b**, Measured compressibility as a function of interlayer tunnelling amplitude t_{\perp} at $U/t \approx 8$. The error bars denote the standard deviation. The shaded region shows the DQMC calculations for a temperature range of $k_B T = 1.0t - 1.4t$.

tomography. For the dataset presented here, we ensured that the contributions from neighbouring planes are negligible.

We observe that the antiferromagnetic intralayer correlations disappear for increasing coupling t_{\perp} between the two-dimensional layers. This result is in stark contrast to the full three-dimensional Hubbard model, where antiferromagnetic correlations in all directions are enhanced by a higher coordination number than in two dimensions, which, together with reduced quantum fluctuations, leads to a phase transition at finite temperature²⁰. However, for a bilayer system, an increasing t_{\perp} has been theoretically predicted^{9,11–15} to drive the formation of singlets across the bonds between the two layers at the expense of reducing magnetic correlations within the layers, as we demonstrate experimentally.

We measure the interlayer magnetic correlations using the technique shown in Fig. 3a (ref. 21). After creating the bilayer system, we rapidly freeze the motion in the x - y layers and thereby effectively create an array of separated double wells along the z axis. Each double well can be occupied by up to four fermions. At half-filling, the large majority of double wells will be in either a spin-singlet state, $(|\uparrow, \downarrow\rangle - |\downarrow, \uparrow\rangle) / \sqrt{2}$, or a triplet state, $\{|\uparrow, \uparrow\rangle, (|\uparrow, \downarrow\rangle + |\downarrow, \uparrow\rangle) / \sqrt{2}, |\downarrow, \downarrow\rangle\}$, which we will discuss as an example—however, the conclusion from the following argument is valid for any occupation. By adiabatically reducing the potential barrier between the two wells, the separated atoms merge into a single well. To maintain the overall anti-symmetry of the two-fermion wave function, only the antisymmetric spin-singlet state merges into the vibrational ground states. By contrast, when merging a spin-triplet state, one atom ends up in a higher vibrational level of the lattice. We distinguish the two outcomes and determine the

probability of a doubly occupied vibrational ground state by performing radiofrequency spectroscopy, which resolves the on-site interaction shift U (ref. 21), combined with in situ imaging. After subtracting the average double occupancy in both measured layers without merging, the density of doubles is proportional to the probability p_{dimer} of antiferromagnetic spin-singlets along a bond between the coupled layers. This probability is converted into a staggered spin correlator of $C_z = -\langle \hat{S}_{i1}^z \hat{S}_{i2}^z \rangle - \langle \hat{S}_{i1}^z \rangle \langle \hat{S}_{i2}^z \rangle = p_{\text{dimer}}/4$. The factor 1/4 results from the consideration that if each bond is occupied by a singlet state, the spin correlator between the layers should match the double-well expectation value of $C_z = 1/4$.

Figure 3b shows the measured interlayer correlations as a function of t_{\perp} . We observe that increasing t_{\perp} enhances the interlayer correlations, which is a key feature of the band insulator phase. Furthermore, they show the opposite behaviour to that of the intralayer correlations shown in Fig. 2b. Therefore, we conclude that by tuning the interlayer coupling, we observe the crossover from the antiferromagnetic Mott insulator to the band insulator.

Finally, in Fig. 4 we show how the crossover depends on the interaction strength U . To this end, we analyse the ratio of total intralayer correlations C_{xy} and interlayer correlations C_z , $R = C_{xy}/(C_{xy} + C_z)$. The total intralayer correlations are defined as $C_{xy} = 2[S(\mathbf{q} = (\pi/d, \pi/d)) - C_0]$, where we subtract the local moment from the staggered spin structure factor in order to take into account only non-local spin correlations, and multiply by a factor of 2 to account for the two layers. The ratio R ranges from 1, for purely intralayer magnetic correlations, to 0 for purely interlayer correlations. The results show a crossover between the limits. We interpolated the data to extract the value of $R = 0.5$, which we show as crosses in the figure. From this, we conclude that the crossover occurs at $t_{\perp}/t \approx 2.5$, with only a weak dependence on the interaction strength. Results from numerical simulations²² show a similar behaviour.

We further investigate the insulating character of the bilayer system for varying t_{\perp} . By applying an in-plane magnetic field gradient of strength $|\nabla B_z| = 24.8 \text{ G m}^{-1}$ and according to the local-density approximation, we extract the filling factor n of a single layer for different chemical potentials. With this, we can calculate the isothermal compressibility $\kappa = \partial n / \partial \mu$ close to half-filling. Our results show an increasingly insulating nature when approaching the band insulating state at high t_{\perp} and agree with DQMC calculations.

Our work shows that strongly interacting lattice systems composed of coupled layers show qualitatively different regimes compared to the two-dimensional Hubbard model. The insights and methodology developed here open the way towards quantum simulations of real materials and, with modifications to the intralayer lattices, of bilayer Haldane models or stacked graphene-like materials.

Online content

Any methods, additional references, Nature Research reporting summaries, source data, extended data, supplementary information, acknowledgements, peer review information; details of author contributions and competing interests; and statements of data and code availability are available at <https://doi.org/10.1038/s41586-020-03058-x>.

- Greif, D. et al. Site-resolved imaging of a fermionic Mott insulator. *Science* **351**, 953–957 (2016).
- Cheuk, L. W. et al. Observation of 2D fermionic Mott insulators of ^{40}K with single-site resolution. *Phys. Rev. Lett.* **116**, 235301 (2016).
- Cocchi, E. et al. Equation of state of the two-dimensional Hubbard model. *Phys. Rev. Lett.* **116**, 175301 (2016).
- Cheuk, L. W. et al. Observation of spatial charge and spin correlations in the 2D Fermi–Hubbard model. *Science* **353**, 1260–1264 (2016).
- Parsons, M. F. et al. Site-resolved measurement of the spin-correlation function in the Fermi–Hubbard model. *Science* **353**, 1253–1256 (2016).
- Drewes, J. H. et al. Antiferromagnetic correlations in two-dimensional fermionic Mott-insulating and metallic phases. *Phys. Rev. Lett.* **118**, 170401 (2017).
- Mazurenko, A. et al. A cold-atom Fermi–Hubbard antiferromagnet. *Nature* **545**, 462–466 (2017).
- Mitra, D. et al. Quantum gas microscopy of an attractive Fermi–Hubbard system. *Nat. Phys.* **14**, 173–177 (2018).
- Scalettar, R. T., Cannon, J. W., Scalapino, D. J. & Sugar, R. L. Magnetic and pairing correlations in coupled Hubbard planes. *Phys. Rev. B* **50**, 13419–13427 (1994).
- Maier, T. A. & Scalapino, D. Pair structure and the pairing interaction in a bilayer Hubbard model for unconventional superconductivity. *Phys. Rev. B* **84**, 180513 (2011).
- Kancharla, S. S. & Okamoto, S. Band insulator to Mott insulator transition in a bilayer Hubbard model. *Phys. Rev. B* **75**, 193103 (2007).
- Golor, M., Reckling, T., Classen, L., Scherer, M. M. & Wessel, S. Ground-state phase diagram of the half-filled bilayer Hubbard model. *Phys. Rev. B* **90**, 195131 (2014).
- dos Santos, R. R. Magnetism and pairing in Hubbard bilayers. *Phys. Rev. B* **51**, 15540–15546 (1995).
- Rüger, R., Tocchio, L. F., Valenti, R. & Gros, C. The phase diagram of the square lattice bilayer Hubbard model: a variational Monte Carlo study. *New J. Phys.* **16**, 033010 (2014).
- Sandvik, A. & Scalapino, D. Order–disorder transition in a two-layer quantum antiferromagnet. *Phys. Rev. Lett.* **72**, 2777–2780 (1994).
- Hafermann, H., Katsnelson, M. & Lichtenstein, A. Metal–insulator transition by suppression of spin fluctuations. *Europhys. Lett.* **85**, 37006 (2009).
- Koepsell, J. et al. Robust bilayer charge-pumping for spin- and density-resolved quantum gas microscopy. *Phys. Rev. Lett.* **125**, 010403 (2020).
- Hartke, T., Oreg, B., Jia, N. & Zwierlein, M. Doubly-hole correlations and fluctuation thermometry in a Fermi–Hubbard gas. *Phys. Rev. Lett.* **125**, 113601 (2020).
- Wurz, N. et al. Coherent manipulation of spin correlations in the Hubbard model. *Phys. Rev. A* **97**, 051602 (2018).
- Scalettar, R. T. Magnetism and spin liquid behavior in a two layer Hubbard model. *J. Low Temp. Phys.* **99**, 499–504 (1995).
- Greif, D., Uehlinger, T., Jotzu, G., Tarruell, L. & Esslinger, T. Short-range quantum magnetism of ultracold fermions in an optical lattice. *Science* **340**, 1307–1310 (2013).
- Bouadim, K., Batrouni, G. G., Hébert, F. & Scalettar, R. Magnetic and transport properties of a coupled Hubbard bilayer with electron and hole doping. *Phys. Rev. B* **77**, 144527 (2008).

Publisher's note Springer Nature remains neutral with regard to jurisdictional claims in published maps and institutional affiliations.

© The Author(s), under exclusive licence to Springer Nature Limited 2020

Methods

Bilayer Hubbard Hamiltonian

The Hamiltonian describing our system contains the tunnelling amplitude t between neighbouring sites i and j of the same layer m , as well as the tunnelling amplitude between the two layers, t_\perp .

$$\hat{H} = -t \sum_{\langle ij \rangle m, \sigma} \hat{c}_{im, \sigma}^\dagger \hat{c}_{jm, \sigma} - t_\perp \sum_{i, \sigma} (\hat{c}_{i1, \sigma}^\dagger \hat{c}_{i2, \sigma} + \text{h.c.}) + U \sum_{im} \hat{n}_{im, \uparrow} \hat{n}_{im, \downarrow} - \mu \sum_{im, \sigma} \hat{n}_{im, \sigma}.$$

Here, $\hat{c}_{im, \sigma}^\dagger$ denotes the creation operator at lattice site i in layer m with spin σ . Doubly occupied sites experience a shift in energy U . The chemical potential μ fixes the average filling factor $\langle \hat{n}_{im, \sigma} \rangle$, where $n_{im, \sigma}$ describes the density at lattice site im in spin state σ .

Loading the bilayer

Initially, we prepare a band insulator of two spin states encoded in the two lowest hyperfine states of ^{40}K , $|\uparrow\rangle = |F=9/2, m_F=-9/2\rangle$ and $|\downarrow\rangle = |F=9/2, m_F=-7/2\rangle$, at attractive interactions of $U/t=-1.7$. This ensures a high occupation of $n=0.95$ per lattice site. For this preparation, the phase between the superlattices is adjusted so that only every second layer of the lattice is populated and tunnelling to neighbouring layers is suppressed. Additionally, during the lattice loading, we ramp up an optical potential created by the spatial light modulator at the outer regions of the atomic cloud to increase the density at the centre. Subsequently, we freeze the density distribution of the band insulator by quickly increasing the intralayer (x - y) lattice depth. To prepare a repulsively interacting gas, we apply a radiofrequency pulse on the $|F=9/2, m_F=-7/2\rangle \rightarrow |F=9/2, m_F=-5/2\rangle$ transition, ramp the magnetic field below the Feshbach resonance of the $|F=9/2, m_F=-9/2\rangle/|F=9/2, m_F=-7/2\rangle$ states and apply a second radiofrequency pulse for the conversion $|F=9/2, m_F=-5/2\rangle \rightarrow |F=9/2, m_F=-7/2\rangle$. The filling factor is reduced to $n=0.9$ upon transferring the band insulator from attractive to repulsive interactions. Subsequently, we shift the superlattice phase closer to the symmetry point and increase the power of the short-wavelength z lattice, which slowly splits the band insulator into a bilayer lattice close to half-filling. The choice of the final superlattice phase allows us to adjust and correct any potential energy offset between the two layers, for example, gravitational sag.

Tomographic in situ imaging of a single layer

After preparing the atoms in the stack of bilayer systems, we freeze their motion by ramping up the horizontal lattice depth in $150\text{ }\mu\text{s}$ to a value of $60E_r$ and simultaneously the short-wavelength z lattice to $110E_r$. To detect a single two-dimensional layer, a strong vertical magnetic field gradient in the z direction is applied, allowing us to resolve the magnetic-field-sensitive hyperfine transition frequencies of the layers. Using radiofrequency tomography, the atoms of one layer are then transferred to another internal state for detection. Subsequently, we implement a spin- and density-resolved detection protocol for the measurement of the intra- and interlayer spin correlations, respectively. For the interlayer correlations, we need to distinguish singly and doubly occupied sites, which we achieve with another radiofrequency transfer that resolves the difference in on-site interaction between initial and final state of 1.8 kHz . For the intralayer correlations, we use a spin-resolved measurement, making use of the spin-changing collision between $|F=9/2, m_F=-9/2\rangle$ and $|F=9/2, m_F=-3/2\rangle$ to remove doubly occupied sites. Finally, absorption images of singles and doubles or spin-up and spin-down singles are taken^{3,6}.

Calibration of Hubbard parameters

We characterize the Hubbard parameter U in the final lattice configuration by radiofrequency spectroscopy of the energy shift caused by

on-site interactions. We observe a 20% decrease in U going from low to high t_\perp , due to the decreased compression of the Wannier wave function. Additionally, we calibrate the tunnelling amplitude t_\perp and the energy offset Δ of the double well using a spin-polarized atomic cloud in a deep x - y lattice, forming separated double wells in the z direction. Initially, we populate only one well of the double-well configuration, before quickly reducing the intensity of the short-wavelength z lattice in order to induce Rabi tunnel oscillations.

Structure factor measurement

In our experiment we measure the two-dimensional spin structure factor at wave vector \mathbf{q}

$$S(\mathbf{q}) = \frac{1}{N} \sum_{i,j} e^{-i\mathbf{q} \cdot \mathbf{r}_{ij}} C_{ij}^z$$

within each layer of the bilayer system^{6,19}. Here, $\mathbf{r}_{ij} = \mathbf{r}_j - \mathbf{r}_i$ is the distance between lattice sites i and j , N is the number of lattice sites, and $C_{ij}^z = \langle \hat{S}_i^z \hat{S}_j^z \rangle - \langle \hat{S}_i^z \rangle \langle \hat{S}_j^z \rangle$ denotes the spin correlator between sites i and j . The operator $\hat{S}_j^z = (\hat{n}_{j,\uparrow} - \hat{n}_{j,\downarrow})/2$ defines the on-site magnetization.

The uniform structure factor $S[\mathbf{q}=(0,0)]$ is determined by the autocorrelation analysis of the difference of two absorption images of the spin-up and spin-down densities taken in one realization of the experiment. The staggered magnetic structure factor at wave vector $\mathbf{q}=(\pi/d, \pi/d)$ is measured by using the spin-spiral imprinting technique discussed in the main text. By contrast, the local moment is directly inferred from the density of the singles, given that only singly occupied sites add to the local magnetization, hence the local moment is $C_{00} = (\langle \hat{S}_\uparrow \rangle + \langle \hat{S}_\downarrow \rangle)/4$. The staggered and uniform structure factor will approach this value once the off-site correlators go to zero in an uncorrelated system, for example, at high temperature.

DQMC simulation

The DQMC simulations are performed using the Quantum Electron Simulation Toolbox (QUEST) Fortran package²³. Simulations are typically performed for a homogeneous lattice with $8 \times 8 \times 2$ sites with 2,000 warm-up sweeps and 200,000 measurement sweeps, and the number of imaginary time slices is set to 25. For the numerical data shown in the main text, the interlayer tunnelling is varied from $t_\perp/t=0$ to 4.5 and on-site repulsion is varied from $U/t=2$ to 8. A small doping is introduced by varying the chemical potential over the range of $\mu/t=0$ to -2.5 , which approximately corresponds to a filling factor ranging from $n=0.5$ to 0.4 . The magnetic structure factor is obtained by a finite Fourier transform of the spatial spin correlators.

Data availability

The data presented in the figures are available at <https://osf.io/u9wj6>. More detailed data and information of this study are available from the corresponding author upon request.

Code availability

The DQMC theory simulations were performed using the QUEST Fortran 90/95 package, version 1.44, from <https://code.google.com/archive/p/quest-qmc/>.

23. Varney, C. N. et al. Quantum Monte Carlo study of the two-dimensional fermion Hubbard model. *Phys. Rev. B* **80**, 075116 (2009).

Acknowledgements This work has been supported by BCGS, the Alexander-von-Humboldt Stiftung, DFG (SFB/TR 185 project B4), Cluster of Excellence Matter and Light for Quantum Computing (ML4Q) EXC 2004/1 - 390534769 and Stiftung der deutschen Wirtschaft.

Author contributions The idea for the experiment was conceived by M.G., N.W., C.F.C. and M.K. Data taking was performed by M.G., N.W. and C.F.C. with contributions by J.S. Data analysis was

primarily performed by M.G. and N.W. Numerical simulations were performed by C.F.C. and N.W. The results were discussed and interpreted by all coauthors, and the manuscript was written by M.K. with contributions from all coauthors.

Competing interests The authors declare no competing interests.

Additional information

Correspondence and requests for materials should be addressed to M.K.

Peer review information *Nature* thanks the anonymous reviewer(s) for their contribution to the peer review of this work.

Reprints and permissions information is available at <http://www.nature.com/reprints>.